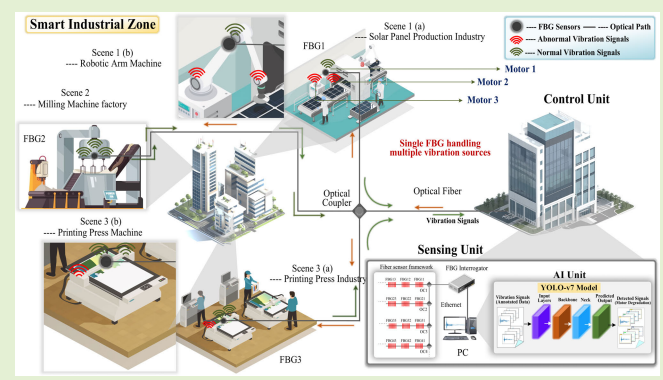


# YOLO-v7 Improved With Adan Optimizer: Realizing Orphaned Fiber Bragg Grating to Sense Superimposed Personalized Dynamic Strain

Pradeep Kumar<sup>ID</sup>, Cheng-Kai Yao<sup>ID</sup>, Michael Augustine Arockiyadoss<sup>ID</sup>, Amare Mulatие Dehnaw, Ching-Yuan Chang, and Peng-Chun Peng<sup>ID</sup>

**Abstract**—In recent years, condition monitoring has become the leading method for diagnosing the health of motor-based machines, with motor vibration or strain being a critical parameter for assessing machine health and detecting abnormal vibrations in multiple running motors posing a significant challenge. This article presents a novel approach to condition monitoring of motors that ensures the prevention of motor wear, reduces high maintenance costs, and increases the durability of machines. The method uses a single fiber Bragg grating (FBG) sensor to sense the vibrations of three electrical motors, and you only look once version 7 (YOLO-v7) as the signal detection algorithm. The Adan optimization technique is used to enhance the YOLO-v7 performance. A maximum of eight possible cases of normal and abnormal dynamic strain can be generated by these three motors operating simultaneously. YOLO-v7 ensures and evaluates the normal and abnormal signals of each motor. The detection result demonstrates the model accuracy of 98.4%. The model performance shows that strains from the motor machine are accurately detected, indicating anomalies. Thus, our proposed experimental setup is flexible, cost-effective, robust, less computation, fast, and improves the sensing quality in anomalies in machine conditioning monitoring.

**Index Terms**—Condition monitoring, dynamic strain, multiple motor-based machines, single fiber Bragg grating (FBG) sensor, you only look once version 7 (YOLO-v7).



## I. INTRODUCTION

IN THIS era, machines function as companions and aids and widely used in every sector of industry such as manufacturing, transportation, automobile, and medical industry [1], [2], [3], [4], [5], [6]. These machines play a vital role in improving

Received 4 September 2024; revised 2 October 2024; accepted 2 October 2024. Date of publication 11 October 2024; date of current version 27 November 2024. This work was supported by the National Science and Technology Council, Taiwan, under Grant NSTC 112-2221-E-027-076-MY2. The associate editor coordinating the review of this article and approving it for publication was Dr. Andre E. Lazzaretti. (*Corresponding author:* Peng-Chun Peng.)

Pradeep Kumar, Cheng-Kai Yao, Michael Augustine Arockiyadoss, Amare Mulatие Dehnaw, and Peng-Chun Peng are with the Department of Electro-Optical Engineering, National Taipei University of Technology, Taipei 10608, Taiwan (e-mail: pcpeng@ntut.edu.tw).

Ching-Yuan Chang is with the Department of Mechanical Engineering, National Taipei University of Technology, Taipei 10608, Taiwan (e-mail: chang@ntut.edu.tw).

Digital Object Identifier 10.1109/JSEN.2024.3474747

human work efficiency. The continuity of work depends on the condition and performance of the machines.

Condition monitoring of the machines is crucial to saving from irreversible damage, especially in critical applications [4], [5], [7], [8], [9], [10]. The method of monitoring and detecting faults in the machine can save time, and the effort of maintenance cause reduces the cost [4]. Fault detection can be a vital factor in improving the durability of the machine [7]. Many parameters can be used to detect faults in electrical equipment such as variations in temperature, vibration, and chemical debris [11], [12], [13]. Vibration variation is a crucial parameter in machines, indicating the initial phase of failures. Such failures can occur at any point during operation or installation. The resultant failure conditions manifest as heavy vibrations, loosened parts, or misalignment in the machine. These fault conditions often arise in bearings [7], [14], [15], [16] leading to irreversible damage and resulting in high maintenance costs. Thus, the noninvasive method is the

preferred method to abstain from breaking the machine without intruding on its operation.

Several studies have been proposed to monitor the condition or health of the motor-based machine using different kinds of sensors [3], [4], [7], [17]. Among these, fiber optic sensors emerged as the most promising outcomes sensor [4]. The application of fiber Bragg grating (FBG) sensors to monitor mechanical machines attracts interest [7]. The advanced FBG sensing approach and features include small size, low mass, high sensitivity, multiphysical, long life, multiplexing, passive characteristic of the sensor, durability in extreme weather conditions, and electromagnetic interference (EMI) immunity [1], [3], [18], [19], [20].

Many previous papers applied the FBG sensor to monitor the health of the machine. Turjo and Lipsett [3] demonstrate the systematic review of retrofitting health and monitoring (HUMS) for unmanned aerial vehicles (UAVs) [21] using an optical fiber sensor. Another study by Biazi-Neta et al. [1] demonstrates the FBG used to monitor the robotic arm motors. The sensors embedded in optical fibers are placed between layers of polyethylene foam and cotton fabric. These studies mostly used vibration as the main parameter to diagnose and detect the faults [14], [16], [22], [23], [24]. The literature from previous studies demonstrates the effective use of multiple FBG sensors to detect faults in industrial machines [1], [22], [23], [24]. In some cases, e.g., a space-constricted object to be tested may only be able to accommodate a single FBG sensor, but that object to be tested may generate multiple sources of vibration. Thus, there is a need to measure multiple vibrations simultaneously using the same FBG. Simultaneous measurement of multiple vibrations with a single FBG maximizes cost-effectiveness, comprehensive monitoring, and space optimization. However, the use of a single FBG sensor for the simultaneous measurement of multiple overlapping personalized dynamic strains is a topic that has not yet been fully explored and resolved.

Furthermore, to enhance detection performance, machine learning is a feasible approach for signal recognition and detection of anomalous or abnormal vibrations or strain [14], [25]. However, traditional algorithms for detecting machine abnormalities face many unresolved challenges. Recently, object detection algorithms have gained prominence due to their lower computation time, high detection scores, and real-time detection capabilities, making them a promising alternative for machine abnormality detection. These are single-stage detectors that have different versions such as YOLO-v1, YOLO-v2, YOLO-v5, and until the popular versions [25], [26]. The architecture of every model is different which provides variation in performance. The YOLO model architecture consists of the following parameters: backbone, neck, and head module. These parameters can vary the performance of the model. With increasing time, performance is increased with improvement in these parameters' networks. The latest version provides the best and optimal performance. The backbone is the vital section which works to fetch the valuable features from the images and creates a feature map. ResNet50, EfficientRep, visual geometry group-16 (VGG-16), and convolutional spatial pyramid darknet-53 (CSP Darknet-53) are common networks that are bound as

backbone networks [26], [27]. The further neck is the mediator between the backbone and the head. The neck consists of the path aggregation network (PAN) and spatial pyramid pooling (SPP) module [26]. The main role of the neck is to associate different networks of the backbone to the feature map. The neck network commonly uses PAN, SPP, Rep-PAN, and neural architecture search-feature pyramid network (NAS-FPN) in the network [26], [28]. The primary responsibility of the head component is to process and associate the features and generate predictions belonging to bounding boxes, classification, and objection prediction results. The bounding boxes in different colors show the prediction results with class labels. Multiscale, efficient decoupled, and anchor-based detection heads are some common heads used in the architecture [29]. However, these previous models have challenges and limitations including low accuracy, high computing cost, 1-D scaling, specific for certain applications, and slower training cause causing more memory usage [26], [30], [31]. To overcome these limitations, you only look once version 7 (YOLO-v7) is combined with the FBG sensing system [25], [32], [33]. The proposed architecture of YOLO-v7 consists of CSP-Darknet as the backbone, extended efficient layer aggregation network (E-ELAN) features [33] and Adam optimizer that provides a high score, decreases the overfitting for different kinds of datasets [34], and solves the problem of data for specific applications.

This article presents a novel approach that uniquely addresses the challenge of recognizing superimposed personalized dynamic strain from various motor-based machines by enhancing the YOLO-v7 algorithm with the Adam optimizer, significantly improving performance. The optimizer is changed in the architecture and only the rest of the structure is similar. The combination of sensor systems and detection algorithms enhances adaptability and sensing quality. The proposed system offers a lower cost and straightforward solution for monitoring strain from motor machines with high sensitivity. Experimental performance demonstrates that our proposed system is capable of enhancing the detection accuracy of faults in machines. In this article, the novelty and contributions are described as follows.

- 1) Our proposed experimental setup uses an orphaned FBG to recognize superimposed personalized dynamic strain from multiple motor-based machines and enhance the sensing structure.
- 2) The proposed YOLO-v7 architecture incorporates the advanced Adam optimizer, which includes the Nesterov momentum algorithm (MA), an adaptive optimization algorithm, decoupled weight decay, and E-ELAN.
- 3) The proposed novel FBG sensing system combined with YOLO-v7 integration enhances training speed, improves detection accuracy, achieves high performance, and mitigates the negative effects of batch size variations.

The rest of this article is organized into the following sections. Section II describes the experimental setup and FBG sensing system. Section III presents the fault detection system, including data collection, labeling, and utilization of YOLO-v7. Section IV showcases the results, encompassing prediction outcomes, and evaluation metrics. Finally, Section V concludes the entire presented article.

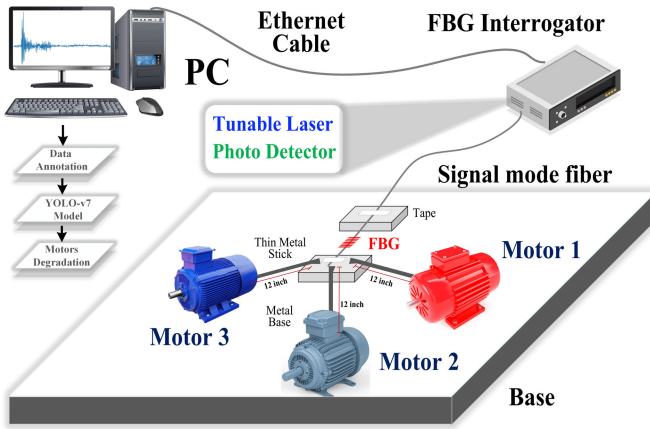


**Fig. 1.** Experimental setup for sensing multimotor strain using a single FBG optical sensor.

## II. EXPERIMENTAL SETUP OF FBG SENSING SYSTEM

This section describes the proposed experimental setup as shown in Fig. 1. The setup contains FBG interrogator of 200-Hz sweep frequency, optical fiber, FBG sensor, personnel computer (PC), and three kinds of universal direct current (dc) electric motors with 200 r/min speed and voltage of 120 V. The FBG interrogator functions as a wavelength sensor, detecting alterations in the reflected light's wavelength from the sensors while optical fiber is the backbone of the sensing system that transmits dynamic strain. The FBG sensor, used for sensing the dynamic strain generated by dc electric motors, actually measures dynamic strain rather than vibration directly. Strain is induced by vibrations, and it is this strain that the FBG sensor detects. The expression for the central wavelength [8], [35] is as follows:

$$\lambda_{\text{Bragg}} = 2 \eta_{\text{eff}} \Lambda \quad (1)$$

where  $\lambda_{\text{Bragg}}$  represents the wavelength satisfying the Bragg condition, while  $\eta_{\text{eff}}$  denotes the effective refractive index of the core fiber.  $\Lambda$  stands for the grating's period or variation in the Bragg wavelength. The extent of strain can be ascertained by observing the shift in the central wavelength, denoted as  $\Delta\lambda$ . This relationship between the central wavelength shift and the strain [14], [36] is expressed as follows:

$$\frac{\Delta\lambda_{\text{Bragg}}}{\lambda} = (1 - p_e)\varepsilon \quad (2)$$

where  $p_e$  represents the elasticity coefficient of the optical fiber, and  $\varepsilon$  denotes the degree of strain.

In this experiment, an FBG sensor is positioned at an optimal location to simultaneously capture dynamic strain from each motor. The optimal placement of the FBG sensor is between two metal bases, with both the endpoints of the optical fiber fixed using plastic tape, as illustrated in Fig. 1. Positioning the sensor between the two bases provides a highly sensitive point for vibration detection. The principle of collecting vibrations from the central metal base is used as a signal source to capture vibrations from a 12-in-long, 0.9-cm-thick elastic stainless steel strip attached to each motor using high-strength epoxy adhesive to ensure no slippage and accurate vibration transmission. Steel is chosen for its high

**TABLE I**  
CASES COVERED DURING EXPERIMENT

Cases	Three Motor Conditions
Case 1	Motor 1 (Normal) Motor 2 (Normal) Motor 3 (Normal)
Case 2	Motor 1 (Normal) Motor 2 (Abnormal) Motor 3 (Abnormal)
Case 3	Motor 1 (Normal) Motor 2 (Normal) Motor 3 (Abnormal)
Case 4	Motor 1 (Normal) Motor 2 (Abnormal) Motor 3 (Normal)
Case 5	Motor 1 (Abnormal) Motor 2 (Normal) Motor 3 (Normal)
Case 6	Motor 1 (Abnormal) Motor 2 (Abnormal) Motor 3 (Abnormal)
Case 7	Motor 1 (Abnormal) Motor 2 (Normal) Motor 3 (Abnormal)
Case 8	Motor 1 (Abnormal) Motor 2 (Abnormal) Motor 3 (Normal)

strength, durability, and excellent ability to transmit vibrations effectively, ensuring accurate and consistent signal capture across all the motors.

Each vibration case is transmitted through an optical fiber, and the interrogator collects the reflected wavelength signals from the FBG sensor every 10 s, ensuring continuous and accurate capture of the vibration data. All the motors are operated under no load conditions, simultaneously under the same conditions and are started and stopped using a switch. Abnormal and normal dynamic strains are caused by this conditional fault such as loosened parts, which generate distinctive abnormal signal patterns from the motors. The motors are assessed for both abnormal and normal vibrations across a maximum of eight cases, as shown in Table I.

These cases illustrate various combinations of normal and abnormal operating conditions across the three motors, highlighting the versatility and effectiveness of the monitoring system in detecting deviations from normal operation. Furthermore, collected data are gathered in the PC that is used in signal detection algorithms. The next section describes the signal detection algorithm.

## III. DYNAMIC STRAIN DETECTION SYSTEM

### A. Data Collection

This section describes a data collection method in which data samples are collected. As shown in Table I, three kinds of motor vibrations are collected in eight maximum possible cases. In all eight cases, dynamic strain showed a different signal according to condition variation in the motor-based machine. The final data are collected in CSV format with numerical values of time and power or amplitude in rows and columns. Then CSV file is converted into.xlsx for converting the image or graphical representation. Method 1 describes the conversion of numerical signal data into video.

Thus, the first method shows the raw column sensing collected data used to plot data from the DataFrame up to the current frame, specifying markers, line style, and marker size. Axes labels, titles, and grids are set accordingly. An animation object is created using FuncAnimation, with the update function, total frames, and frame interval. Finally, the animation is displayed. Then, the second method described the process of converting a video into individual frames. The algorithm first checks for the existence of the output directory; if it is not found, the algorithm creates the folder directory. Subsequently, it opens the specified video file located at the video path, ensuring successful access to the video content. The algorithm then proceeds to read each frame of the video, incrementing the frame count variable. Frames are saved as images in the designated directory at intervals defined by frame internal, with filenames structured as frame(frame count).jpg. Finally, upon completion of frame extraction, the algorithm releases the video object and outputs a message confirming successful conversion, along with the total number of frames converted, denoted by frame count. The final dataset is created in which each class contains 250 frames and the total frames is  $250 \times 8 = 2000$  frames and then processed for annotation. The next section describes data annotation.

### B. Data Annotation

Data annotation is a method in which data are labeled to train the signal detection model. YOLO-v7 is used as a dynamic strain detection model. During labeling, eight cases are covered and annotated as follows: cases 1–8. Finally, each case generated 250 labels with respected frames and a total of eight cases created 2000 labels of which 70% (1400 frames) for training, 20% (400 frames) for validation, and 10% (200 frames) for testing randomly in the same ratio from each case. Furthermore, the final annotated dataset is processed for training and validation in the signal section model.

### C. Signal Detection Algorithm (YOLO-v7)

This section describes the signal detection algorithm, as illustrated in Fig. 2. The previous section detailed the data collection and annotation process, which is crucial since YOLO requires an annotated dataset for model training. The YOLO-v7 architecture consists of four main modules: input, backbone, head, and prediction.

- 1) *Input:* The YOLO-v7 architecture begins with an initial preprocessing step, where input dynamic strain images are resized to  $416 \times 416$  pixels before being fed into the backbone layers.
- 2) *Backbone:* The backbone consists of three main modules: CBS, E-ELAN, and MP1. The learning capacity is enhanced through the E-ELAN module [29]. This module maintains the original ELAN in the architecture, guiding the computation blocks and learning possible features [26], [37]. The CBS module is used for developing the convolution SiLU activation function and batch normalization [38]. MP1 is created by the MaxPool and CBS modules, separated into two sections: top and bottom. The top section uses MaxPool to halve the image

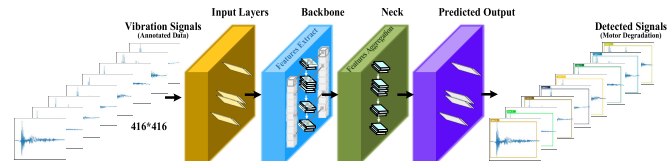


Fig. 2. Degraded dynamic strain detection using Yolo-v7 model.

dimensions and CBS with 128 output channels to halve the image channels. The bottom section halves the image channels through a CBS with a  $1 \times 1$  stride and kernel and halves the image dimensions associated with a CBS of  $2 \times 2$  stride and  $3 \times 3$  kernel [32]. Furthermore, concatenation (Cat) is used to extract from both the sections. MaxPool gathers possible information from localized locations, and CBS collects information from small locations. Therefore, the integration of methods of networks has the ability to extract required features through the input dynamic strain images.

- 3) *Head:* This head network in architecture contains an FPN structure, which uses by PANet design [26]. This network includes multiple convolutional, SiLU activation, batch normalization, and CBS blocks. In addition, it introduces a convolutional SPP and SPP (CSPC-SPP) structure, a MaxPool-2 (MP2), and E-ELAN. The convolutional spatial pyramid (CSP) structure inside the SPP improves the network structure through the cspc-spp structure. As a result, feature extraction and optimization are enhanced. The ELAN-H layer is developed by E-ELAN and several feature layers are based on E-ELAN and improve the feature extraction [32]. Furthermore, there are two MP blocks: MP1 and MP2, which have different numbers of output channels but similar structures.
- 4) *Prediction:* This is the final stage which consists of rep design structure which uses the number of image channels to features of the head structure. The prediction is predicted here through  $1 \times 1$  convolutional as results anchor frame and category are predicted. The Rep structure is inspired by the RepVGG structure [39] that enhances the training process. Thus, the complexity is minimized without affecting the prediction results of dynamic strain.

### D. Adam Optimizer in YOLO-v7

Adam optimizer is a newly developed optimizer by the research team of Singapore Sea Artificial Intelligence Lab (S-SAIL) [40]. This optimizer is used in multiple deep-learning-based frameworks [41] for improving detection accuracy. However the previous optimizer and adaptive gradient algorithms such as Adam, Adam-W, RMSprop, AMSGrad, Adagrad, Adamax, and SGD have limitation [41]. To improve the limitation, this optimizer has been introduced that provides faster optimization and achieves less computation time with higher accuracy during training and validation of the model. Algorithm 1 shows the implementation in the YOLO-v7 framework [42]. The initial steps include inputting the signal image in the backbone to extract the features and then

processing it to the head module. Then next is the optimizer steps process before Adan, Adam, and Adam-W are notable optimizers [41]. These optimizers have traditional convex optimization, and the heavy ball (HB) method is equal to the MA; the Nesterov MA is depicted in the equation below [41]

$$\begin{aligned} AGD : \{g_k &= \nabla f(\theta_k - \eta(1 - \beta_1)m_{k-1}) + \xi_k \\ m_k &= (1 - \beta_1)m_{k-1} + g_k \\ \theta_{k+1} &= \theta_k - \eta m_k\} \end{aligned} \quad (3)$$

where  $g_k$  denotes the stochastic gradient at iteration  $k$ , which is the gradient of the objective function with respect to the model parameters  $\theta_k$  and includes a noise term  $\xi_k$ .  $\eta$  is the step size or learning rate,  $\beta_1$  is the momentum coefficient, and  $m_k$  represents the first moment vector at iteration  $k$ .

The Nesterov MA has a quick rate of convergence in comparison to the HB method for common convex and smooth issues handling larger batch sizes in the theoretical approach. The Nesterov algorithm is different from the HB method, and the Nesterov algorithm does not evaluate the current point gradient, but it uses the momentum to obtain the projection point and further maintains momentum accumulation after calculating the gradient at that location. The Nesterov algorithm rarely initiated in-depth optimizer and Nesterov MA. Evaluating the gradient at projected points is a major reason, so it needs diverse overloading of model factors at the time of improvement at current points and needs backpropagation at projected points, which has many benefits. These drawbacks significantly restrict the use of the Nesterov MA in deep model optimization.

Then the Adan researcher obtained the latest optimizer of Adan by associating improved Nesterov momentum with adaptive optimization and developed the decoupled weight attenuation process. Thus, the diverse model factor issue is solved in Nesterov MA [41], and the rewriting algorithm is as follows:

#### Reformulated AGD

$$\begin{aligned} \{g_k &= E_{\zeta \sim D}[\nabla f(\theta_k, \zeta)] + \xi_k \\ m_k &= (1 - \beta_1)m_{k-1} + [g_k + (1 - \beta_1)(g_k - g_{k-1})] \\ \theta_{k+1} &= \theta_k - \eta m_k\} \end{aligned} \quad (4)$$

where  $g_k$  is the stochastic gradient at iteration  $k$ , which is now expected over the distribution  $D$  with respect to sample  $\zeta$ .  $\nabla f(\theta_k, \zeta)$  represents the gradient of the objective function with respect to  $\theta_k$  for sample  $\zeta$ .

The above MA includes the adaptive class optimizer with the updated  $m_k$  shifts to moving average form from cumulative form and incorporates the second-order moment to adjust the learning rate, which has led to the basic version of Adan's algorithm [41]. The expression is depicted below

#### Vanilla Adan

$$\begin{aligned} \{m_k &= (1 - \beta_1)m_{k-1} + \beta_1[g_k + (1 - \beta_1)(g_k - g_{k-1})] \\ n_k &= (1 - \beta_3)n_{k-1} + \beta_3[g_k + (1 - \beta_1)(g_k - g_{k-1})]^2 \\ \eta_k &= \frac{\eta}{\sqrt{n_k + \epsilon}} \\ \theta_{k+1} &= \theta_k - \eta_k \circ m_k\} \end{aligned} \quad (5)$$

---

#### Algorithm 1 YOLO-v7 With Adan Optimizer

---

- 1: **Input:** An image  $[L \times B \times 3]$ .
  - 2: **Output:** Dynamic Strain Detection.
  - 3: **Preprocessing:** The input signal image of size  $416 \times 416$ .
  - 4: **Process of model training:**
  - 5: **for** every signal image in the training set **do**
  - 6:     **Stage 1:** The processed signal images undergo feature extraction within the backbone module, which subsequently produces three feature maps at varying scales. These feature maps are then collectively fed inside the head module for prediction.
  - 7:     **Stage 2:** In the head module, a fusion of three kinds of feature maps occurs, which are then passed into the RepVGG block and detect block for object prediction.
  - 8:     **Stage 3:** The loss function module computes the inference loss based on the disparity between the model output and the actual label. Following this, the model derives the gradient from the loss and forwards it to the optimizer module.
  - 9:     **Stage 4:** Adan Optimizer initiates with the given parameters: initialization 0, step size  $n$ , average parameter  $(\beta_1, \beta_2, \beta_3, \beta_3 \in [0, 1]^3)$ , stable parameter, weight decay  $\epsilon > 0$ , and restart condition  $\lambda_k > 0$ , and then intimate the optimizing method.
  - 10:     **for**  $k < K$  **do**
  - 11:         Evaluate the stochastic gradient estimator  $g_k$  at  $\theta_k$ ;
  - 12:          $m_k = (1 - \beta_1)m_{k-1} + \beta_1 g_k$  /\* (set  $m_0 = g_0$ ) \*/;
  - 13:          $v_k = (1 - \beta_2)v_{k-1} + \beta_2(g_k - g_{k-1})$  /\*set  $v_1 = g_1 - g_0$  \*/;
  - 14:          $n_k = (1 - \beta_3)n_{k-1} + \beta_3[g_k + (1 - \beta_1)(g_k - g_{k-1})]^2$ ;
  - 15:          $n_k = \eta / \sqrt{n_{k-1} + \epsilon}$ ;
  - 16:          $\theta_{k+1} = (1 + \lambda_k \eta)^{-1}[\theta_k - \eta_k(m_k + (1 - \beta_2)v_k)]$ ;
  - 17:         **if** restart condition holds **then**
  - 18:             get stochastic gradient estimator  $g_0$  at  $\theta_k + 1$ ;
  - 19:              $m_0 = g_0$ ,  $v_0 = 0$ ,  $n_0 = (g_0)^2$ , update  $\theta_1$  by Line 15,  $k = 1$ ;
  - 20:         **end if**
  - 21:     **end for**
  - 22: **end for**
- 

where  $m_k$  is the first moment vector adjusted to incorporate the gradient difference, while  $n_k$  represents the second moment vector used for adjusting the learning rate.  $\beta_3$  is the momentum coefficient for the second moment,  $\eta_k$  is the adjusted step size, and  $\epsilon$  is a small constant added for numerical stability.

The variated  $m_k$  is seen to combine the gradients with variate gradients and in real-world applications. Thus, there is often a frequent need to address the two physically distinct meaningful factors separately. That is why, gradient difference momentum  $v_k$  is developed by researchers [41] as depicted in the expression

$$\begin{aligned} m_k &= (1 - \beta_1)m_{k-1} + \beta_1 g_k, \\ v_k &= (1 - \beta_2)v_{k-1} + \beta_2(g_k - g_{k-1}) \end{aligned} \quad (6)$$

**TABLE II**  
YOLO-v7 MODEL TRAINING PARAMETERS

Parameter	Configuration
Image Size	416 × 416
Learning Rate	$1 \times 10^{-3}$
Batch Size	8
Validation Split	0.2
Optimizer	Adan
Weight Decay	0.002
Epochs	400
Training Period	4 hours

where  $v_k$  is the gradient difference momentum that captures the difference between successive gradients.  $\beta_2$  is a momentum coefficient for the gradient difference.

The weight attenuation method is introduced by Adan based on L2 regular decoupling. In each iteration of Adan, the process can be seen as minimizing a first-order approximation of the optimization objective F [41] as depicted below

$$\begin{aligned}\theta_{k+1} &= \theta_k - \eta_k \circ \bar{m}_k \\ &= \underset{\theta}{\operatorname{argmin}} \left( F(\theta_k) + \langle \bar{m}_k, \beta - \theta_k \rangle + \frac{1}{2\eta} \|\theta - \theta_k\|_{\sqrt{n_k}}^2 \right)\end{aligned}$$

where

$$\begin{aligned}\|x\|_{\sqrt{n_k}}^2 &:= \langle x, \sqrt{n_k + \epsilon} \circ x \rangle \\ \bar{m}_k &:= m_k + (1 - \beta_2)v_k\end{aligned}\quad (7)$$

where  $\bar{m}_k$  is a combined term of  $m_k$  and  $(1 - \beta_2)v_k$ . The term  $\|x\|_{\sqrt{n_k}}^2$  denotes the weighted norm with  $\sqrt{n_k + \epsilon}$ .

The gradient momentum and gradient sets the mean coefficient or variate momentum. The gradient can affect the optimizer speed causing slow due to inconsistent adjacent gradients, and similar path flow can increase the performance speed.

It is seen that the first-order approximation is not relevant, and F in L2 weight regularization (WR) is smooth and simple. Thus, L2 WR is unnecessary to process and the first-order approximation can be processed [41]. The final step of Adan can be obtained as noted and expressed as

$$\begin{aligned}\theta_{k+1} &= \theta_k - \eta_k \circ \bar{m}_k \\ &= \underset{\theta}{\operatorname{argmin}} F(\theta_k) + \bar{m}_k, \theta - l\theta_k + \frac{1}{2\eta} \|\theta - \theta_k\|_{\sqrt{n_k}}^2.\end{aligned}\quad (8)$$

The main algorithm is obtained by associating the two above mathematical equations' enhancement (6) and (8) into the ground version of Adan. These parameters  $v_k, n_k, m_k$ , etc. are used to process YOLO-v7 model training and minimize the loss to obtain higher detection results.

Furthermore, the YOLO-v7 model was trained using a system with the following specifications: an Intel<sup>1</sup> Core<sup>2</sup> i7-9700k CPU running at 3.60 GHz, 16 GB of RAM, and an NVIDIA GeForce RTX 2080Ti with CUDA 11.8. For the implementation, the model used PyTorch and Python libraries. The table shows the hyperparameters as shown in Table II used to obtain optimal performance. The next subsequent section

provides the prediction results and evaluation metrics of the detection model.

## IV. RESULTS

This is the result section which provides the performance of the signal detection algorithm with optimal parameters that show the performance on validation samples; a further section describes the evaluation metrics and prediction result of YOLO-v7 as outlined below.

### A. Prediction of Faulty Signal Detection of YOLO-v7

This section provides the performance of the detection algorithm for abnormal and normal vibration conditions on test datasets. Fig. 3 depicts the abnormal and normal vibration prediction results of the motor-based machine. The bounding boxes present abnormal and normal vibrations of three motors schematically. The analysis of vibration prediction results for the motor-based machine reveals distinct patterns in each case. Each case vibration is a combined condition of the vibrations from three motors as in Fig. 3. The prediction of case 1 shows that all three motors are in normal operating conditions, indicative of optimal functionality. Conversely, case 2 demonstrates abnormalities in motors 2 and 3, while motor 1 prediction shows normal condition. Similarly, case 3 depicts normal functioning for motors 1 and 2, with abnormalities observed in motor 3. In case 4, motor 2 shows deviations from normal conditions, while motors 1 and 3 operate within expected ranges. Case 5 highlights abnormal vibration in motor 1, while motors 2 and 3 function normally. In case 6, all three motors exhibit abnormal conditions, suggesting systemic issues. Case 7 predicts abnormalities in motors 1 and 3, with motor 2 remaining within the normal condition. The final case 8 predicts abnormalities in motors 1 and 2, while motor 3 condition is normal. These findings emphasize the importance of continuous monitoring and maintenance to ensure the optimal performance and longevity of motor-based systems. The detailed evaluation results follow in the subsequent section, offering an in-depth analysis and comprehensive insights.

### B. Evaluation Metrics Analysis of Signal Detection Model on Dynamic Strain

This section provides evaluation metrics of the proposed model on the vibration dataset. The evaluation metrics provide precision scores, recall scores, average precision, mean average precision (mAP), and other valuable metrics to show the performance of the proposed model. Precision evaluates the accuracy of the positive predictions. It is defined as the ratio of true positive (TP) predictions to the total number of false positive (FP) and TP predictions made by the model [25] as shown in the expression below

$$\text{Precision} = \frac{\text{True Positives}}{\text{True Positives} + \text{False Positives}}.\quad (9)$$

Recall evaluates the completeness of the positive predictions. It is expressed as the ratio of TP predictions to the total

<sup>1</sup>Registered trademark.

<sup>2</sup>Trademarked.

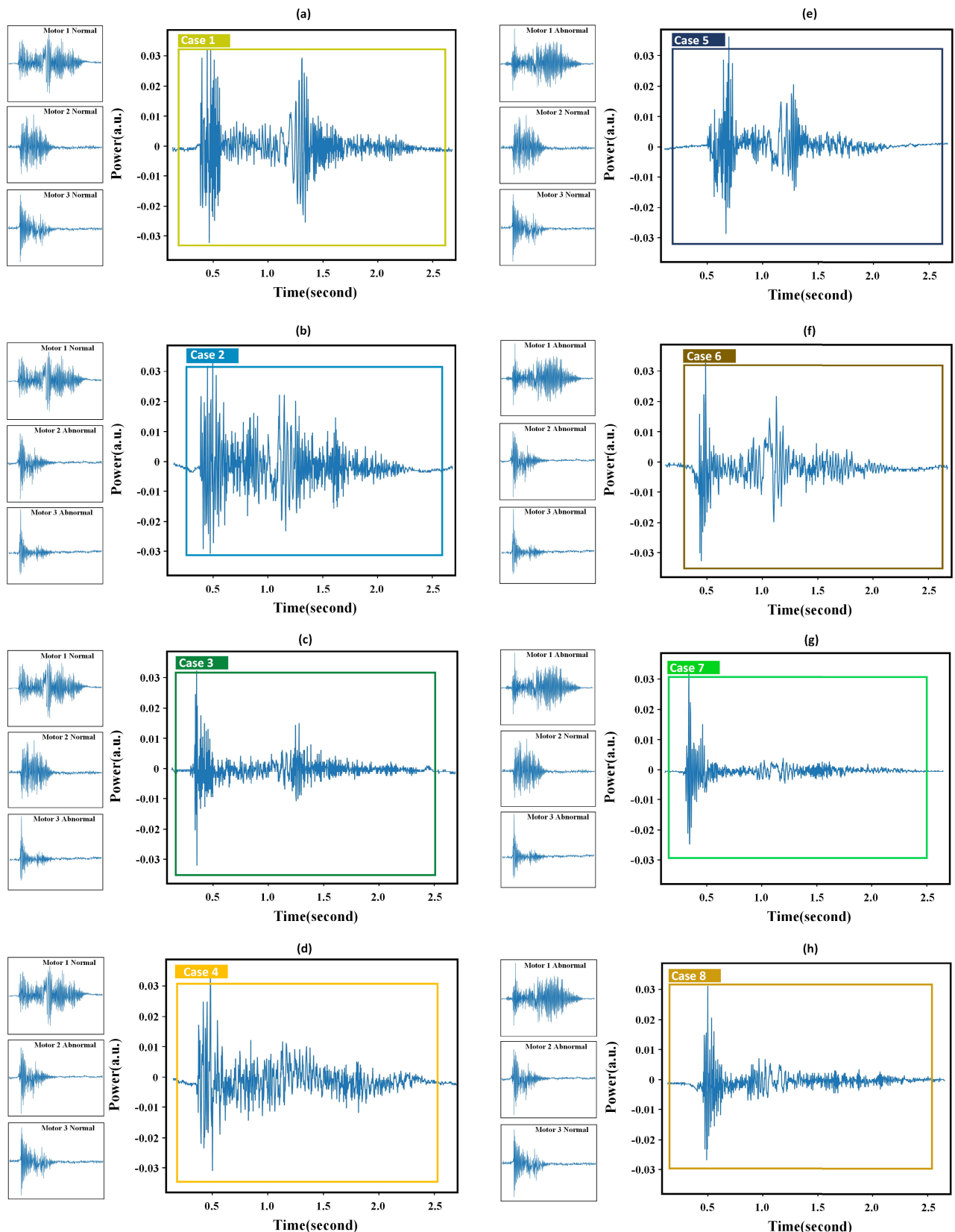


**Fig. 3.** Prediction performance of the proposed model in eight conditions of machine. (a) Case 1 predicts condition of motor 1 (normal), motor 2 (normal), and motor 3 (normal). (b) Case 2 predicts condition of motor 1 (normal), motor 2 (abnormal), and motor 3 (abnormal). (c) Case 3 predicts motor 1 (normal), motor 2 (normal), and motor 3 (abnormal). (d) Case 4 predicts motor 1 (normal), motor 2 (abnormal), motor 3 (normal). (e) Case 5 predicts motor 1 (abnormal), motor 2 (normal), and motor 3 (normal). (f) Case 6 predicts the condition of motor 1 (abnormal), motor 2 (abnormal), motor 3 (abnormal). (g) Case 7 predicts the condition of motor 1 (abnormal), motor 2 (normal), and motor 3 (abnormal). (h) Case 8 predicts the condition of motor 1 (abnormal), motor 2 (abnormal), and motor 3 (normal).

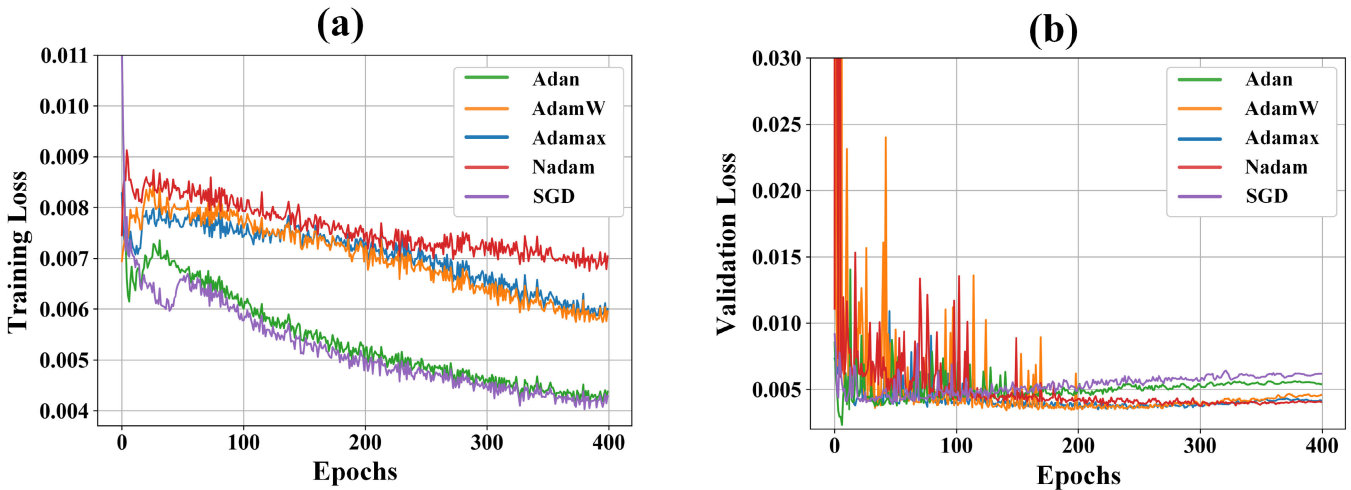


Fig. 4. Comparison loss graphs of various optimizers. (a) Training loss graph. (b) Validation loss graph at various epoch numbers.

number of actual positive instances in samples [25], [29]. The expression can be shown as

$$\text{Recall} = \frac{\text{True Positives}}{\text{True Positives} + \text{False Negatives}}. \quad (10)$$

The mAP is a metric for measuring object detection algorithms which evaluates the average precision for each class across all levels of confidence and then averages those precisions over all classes. Average precision computes the area under the precision-recall curve [29] as shown below

$$\text{AP} = \int_0^1 (\text{precision} \times \text{recall})_k \quad (11)$$

where  $(\text{precision} \times \text{recall})_k$  shows the product of precision and recall at a specific rank  $k$ . Here,  $k$  refers to the specific value. Thus,  $(\text{precision} \times \text{recall})_k$  represents the precision-recall product at that particular rank  $k$  [25], [43]. The below expression represents the mAP as

$$\text{mAP} = \frac{1}{N_{\text{classes}}} \sum_{i=1}^{N_{\text{classes}}} \text{AP}_i \quad (12)$$

where  $N_{\text{classes}}$  is the total number of classes in the dataset. Furthermore, the prediction results are shown below such as confusion matrix, precision-recall curve, loss curve of training and validation, and accuracy graph.

Moreover, Fig. 4 illustrates the loss graphs used to assess model performance with various optimizers. Fig. 4(a) and (b) depicts the training and validation loss curves for AdamW, Adamax, Nadam, and SGD with Adan optimizers. The graphs demonstrate the differences in loss performance among the optimizers, highlighting the impact of each optimizer on convergence rate and overall loss during training and validation. During training, SGD and Adan outperformed the other optimizers, while during validation, Adamax and Nadam showed superior performance. In addition, SGD and Adan proved to be highly stable and faster optimizers throughout the comparison, with Adan also achieving higher accuracy and reducing training time significantly. This analysis underscores the importance of selecting an appropriate optimizer

for different stages of model training, with Adan emerging as a particularly strong candidate for its balance of speed, efficiency, and accuracy. Furthermore, it provides insights into the tradeoffs between training stability and validation performance. Thus, the comparison indicates that the Adan optimizer is particularly effective.

Furthermore, Fig. 5(a) illustrates the accuracy of the proposed model across various parameters. The first section displays the precision curve concerning the number of epochs. It is observed that as the number of epochs increases, the accuracy of the model stabilizes, indicating its robustness. In the second section, the recall curve is depicted. It is noted that during the initial stages, the model exhibits instability in its performance, which gradually improves and stabilizes after reaching half of the total number of epochs. Meanwhile, the other section shows the mAP at different threshold values ranging from 0.5 to 0.95. The curves demonstrate the high-performance detection capabilities of the proposed model.

In addition, Fig. 5(b) exhibits the comprehensive performance of the object detection model throughout the training process, displaying the flow of model training and validation losses in a unified graph. This graph illustrates the trends of the training and validation losses for bounding boxes, objectness, and classification across increasing epochs. It provides insights into how these losses evolve during the training of the model. The main parameters are set as follows: weight decay, optimizer, epochs, batch size, image size, and learning rate are 0.001, Adan, 400, 8, 416 × 416, and  $1 \times 10^{-3}$  respectively. During training, the loss values of the box, objectness, and classification are continuously improving. The loss of box, objectness, and classification during the training process is 0.01, 0.006, and 0.00001, respectively. These results are quite impressive in demonstrating the effectiveness of network's training. Similarly, the validation loss of box, objectness, and classification is 0.01, 0.005, and 0.002, respectively. It is observed that during model training, the model is stable at every epoch number due to the constant decrease of the loss curve. Therefore, our proposed model perfectly detects

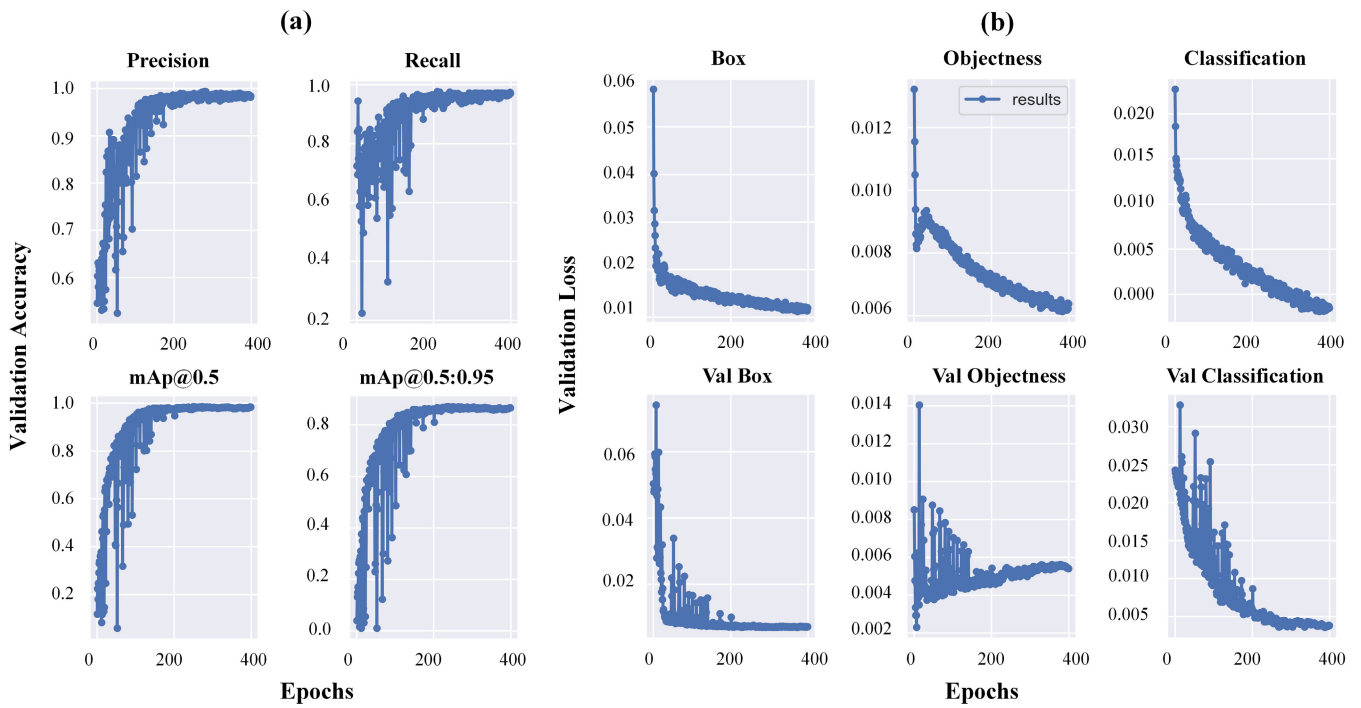


**Fig. 5.** Proposed model validation performance graphs. (a) Accuracy graphs on validation dataset. (b) Training and validation loss graph at various epochs number.

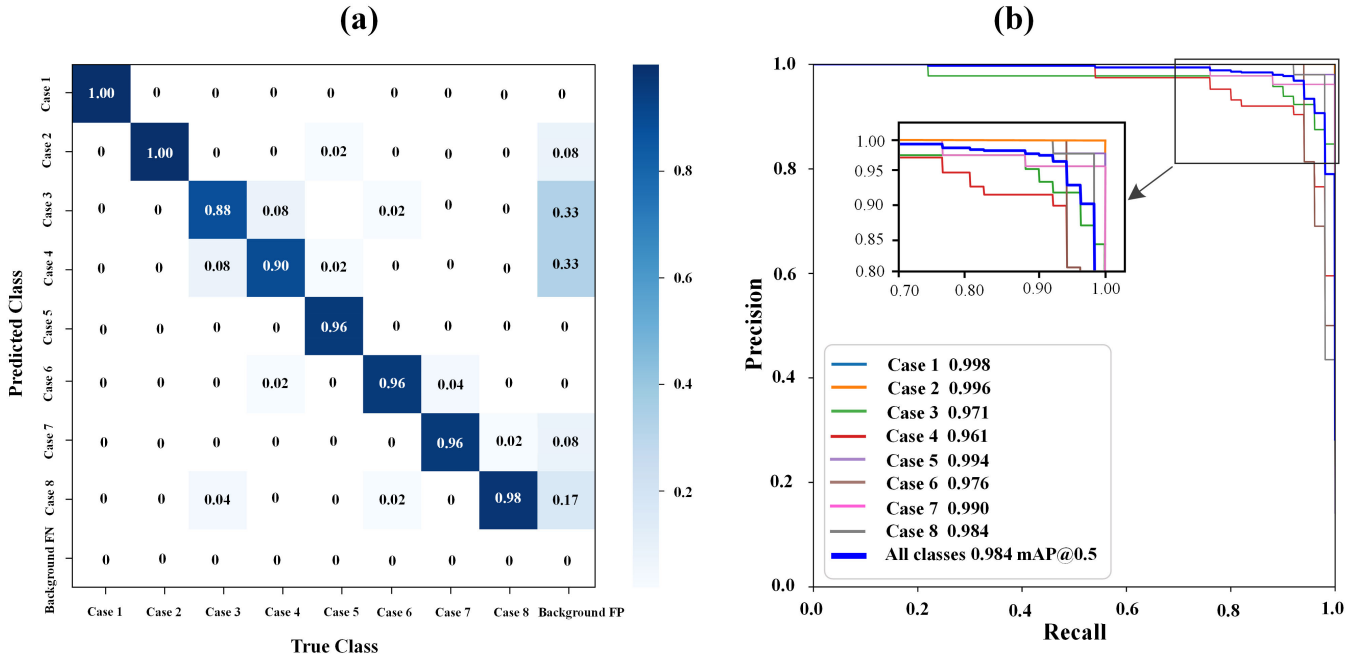


**Fig. 6.** Proposed model matrices on validation dataset. (a) Confusion matrix. (b) Precision–recall curve.

abnormal and normal motor conditions and obtains highly accurate results in comparison to other traditional models, with low loss values.

Fig. 6(a) displays the confusion matrix illustrating the classification results of the model on the validation dataset, showcasing its predictions compared to the ground truth across different classes. Each cell in the matrix represents the accuracy for a specific class, with FN (missed objects) highlighted

in the background, indicating instances where the model failed to detect certain objects, and FP (nonexistent objects) shown in the background, denoting false detection. The precision–recall curve depicted in Fig. 6(b) illustrates the precision (y-axis) and recall (x-axis) for various threshold values. Each class’ accuracy is separately represented on the curve on the validation dataset. The YOLO-v7 model’s curve demonstrates its distinct validation performance in distinguishing between eight

classes: cases 1–8, achieving individual accuracies of 99.8%, 99.6%, 97.1%, 96.1%, 99.4%, 97.6%, 99.0%, and 98.4%, respectively. Section V this article and suggests future research directions.

## V. CONCLUSION AND FUTURE DIRECTION

This article demonstrates the novel approach for condition monitoring of three motors using a single FBG sensor combined with YOLO-v7 for detecting abnormal dynamic strain. The performance of the proposed experimental setup demonstrates that abnormal and normal vibrations of the three simultaneously running motors are effectively sensed. In comparison to the configuration of multiple FBG sensors, the experiment confirmed that the single FBG-based structure is the preferred choice for a reliable and stable vibration FBG sensor system.

Moreover, to address the signals' detection solution, YOLO-v7 with Adam optimizer is used here to detect the dynamic strain in real-time. The model identifies the dynamic strain with high accuracy. The overall mAP or accuracy is 98.4%. Therefore, the proposed system promises to decrease the number of FBG sensors, be cost-oriented, have less computational time, real-time detection, fast deployment, and improve the FBG sensing structure. In addition, the proposed system ensures the improvement of motor conditions by extracting features from dynamic strain. The model can be a suitable tool for various applications in machinery industries to enhance the durability, stability, robustness, and overall monitoring of motor-based machines.

## REFERENCES

- [1] V. Biazi-Neto, C. A. F. Marques, A. Frizera-Neto, and A. G. Leal-Junior, "FBG-based sensing system to improve tactile sensitivity of robotic manipulators working in unstructured environments," *Sens. Actuators A, Phys.*, vol. 359, Sep. 2023, Art. no. 114473.
- [2] M. Fajkus et al., "FBG sensor for heart rate monitoring using 3D printing technology," *IEEE Access*, vol. 12, pp. 57150–57162, 2024.
- [3] I. Turjo and M. G. Lipsett, "Retrofitting health and usage monitoring systems (HUMS) for unmanned aerial vehicles," in *Proc. IEEE Aerosp. Conf.*, Mar. 2023, pp. 1–12.
- [4] M. Aishwarya and R. M. Brisilla, "Design and fault diagnosis of induction motor using ML-based algorithms for EV application," *IEEE Access*, vol. 11, pp. 34186–34197, 2023.
- [5] Q. Liu, Y. Yu, B. S. Han, and W. Zhou, "A novel compact high-sensitivity fiber Bragg grating sensor for microvibration measurement of robot joints," *IEEE Sensors J.*, vol. 24, no. 8, pp. 12385–12399, Apr. 2024.
- [6] R. Jha, P. Mishra, and S. Kumar, "Advancements in optical fiber-based wearable sensors for smart health monitoring," *Biosensors Bioelectron.*, vol. 254, Jun. 2024, Art. no. 116232.
- [7] L. Macedo, P. Louzada, L. G. Villani, A. Frizera, C. Marques, and A. Leal-Junior, "Machinery fault diagnosis in electric motors through mechanical vibration monitoring using fiber Bragg grating-based accelerometers," *IEEE Sensors J.*, vol. 24, no. 13, pp. 20655–20662, Jul. 2024.
- [8] R. C. Lazaro, E. Souza, A. Frizera, C. Marques, and A. Leal-Junior, "Optical fiber sensors systems in oil tanks: Toward structural health monitoring and liquid-level estimation," *IEEE Sensors J.*, vol. 23, no. 10, pp. 10437–10443, May 2023.
- [9] A. Mahlooji and F. Azhari, "A fiber-only optical vibration sensor using off-centered fiber Bragg gratings," *IEEE Sensors J.*, vol. 24, no. 9, pp. 14245–14252, May 2024.
- [10] W. Huang, X. Tong, Y. Mao, Y. Wang, and C. Li, "FBG sensor for rotation speed measurement with large sensing distance based on Terfenol-D," *IEEE Sensors J.*, vol. 23, no. 6, pp. 5786–5794, Mar. 2023.
- [11] A. B. Di Renzo et al., "Edge device for the classification of photovoltaic faults using deep neural networks," *J. Control, Autom. Electr. Syst.*, vol. 35, no. 5, pp. 861–869, Aug. 2024.
- [12] E. H. Dureck et al., "Condition assessment of AC contactors using optical fiber sensors and deep learning," in *Proc. SBMO/IEEE MTT-S Int. Microw. Optoelectron. Conf. (IMOC)*, Nov. 2023, pp. 307–309.
- [13] G. G. Kuhn, K. M. Sousa, C. Martelli, C. A. Bavastri, and J. C. C. da Silva, "Embedded FBG sensors in carbon fiber for vibration and temperature measurement in power transformer iron core," *IEEE Sensors J.*, vol. 20, no. 22, pp. 13403–13410, Nov. 2020.
- [14] B. Brusamarello, J. C. C. da Silva, K. de Morais Sousa, and G. A. Guarneri, "Bearing fault detection in three-phase induction motors using support vector machine and fiber Bragg grating," *IEEE Sensors J.*, vol. 23, no. 5, pp. 4413–4421, Mar. 2023.
- [15] J. de Pelegrin, U. J. Dreyer, K. M. Sousa, and J. C. C. da Silva, "Smart carbon-fiber reinforced polymer optical fiber Bragg grating for monitoring fault detection in bearing," *IEEE Sensors J.*, vol. 22, no. 13, pp. 12921–12929, Jul. 2022.
- [16] A. Mohammed and S. Djurovic, "Electric machine bearing health monitoring and ball fault detection by simultaneous thermo-mechanical fibre optic sensing," *IEEE Trans. Energy Convers.*, vol. 36, no. 1, pp. 71–80, Mar. 2021.
- [17] Kusnandar, D. N. Anggraeni, Kartaman, A. Najmurrokhman, N. Ismail, and M. R. Effendi, "Development of guiding cap for disabilities with limited vision using ultrasonic sensors and vibrating motor disc," in *Proc. 9th Int. Conf. Wireless Telematics (ICWT)*, vol. 4, Jul. 2023, pp. 1–4.
- [18] M. A. Tefera, Y. C. Manie, C.-K. Yao, T.-P. Fan, and P.-C. Peng, "Meta-learning for boosting the sensing quality and utility of FSO-based multichannel FBG sensor system," *IEEE Sensors J.*, vol. 23, no. 24, pp. 31506–31512, Dec. 2023.
- [19] Z. M. Fadlullah and N. Kato, "On smart IoT remote sensing over integrated terrestrial-aerial-space networks: An asynchronous federated learning approach," *IEEE Netw.*, vol. 35, no. 5, pp. 129–135, Sep. 2021.
- [20] L. Macedo, P. Louzada, L. G. Villani, A. Frizera, C. Marques, and A. Leal-Junior, "Fiber Bragg grating-based accelerometer design based on multi-objective optimization," *Opt. Fiber Technol.*, vol. 85, Jul. 2024, Art. no. 103796.
- [21] R. W. Ibrahim, T. K. Rodrigues, and N. Kato, "Impact of UAV failure and severe weather conditions in mmWave and terahertz signals for AeriaL edge computing," in *Proc. IEEE 98th Veh. Technol. Conf. (VTC-Fall)*, Oct. 2023, pp. 1–7.
- [22] C. Mongia, D. Goyal, and S. Sehgal, "Vibration response-based condition monitoring and fault diagnosis of rotary machinery," *Mater. Today, Proc.*, vol. 50, pp. 679–683, Jan. 2022.
- [23] R. P. Linessio, K. de Morais Sousa, T. da Silva, C. A. Bavastri, P. F. da Costa Antunes, and J. C. C. da Silva, "Induction motors vibration monitoring using a biaxial optical fiber accelerometer," *IEEE Sensors J.*, vol. 16, no. 22, pp. 8075–8082, Nov. 2016.
- [24] M. Silveira et al., "A fiber Bragg grating based accelerometer for monitoring the vibration of an industrial engine prototype: A preliminary study," *J. Phys., Conf. Ser.*, vol. 2407, no. 1, Dec. 2022, Art. no. 012039.
- [25] P. Kumar, G.-L. Shih, C.-K. Yao, S. T. Hayle, Y. C. Manie, and P.-C. Peng, "Intelligent vibration monitoring system for smart industry utilizing optical fiber sensor combined with machine learning," *Electronics*, vol. 12, no. 20, p. 4302, Oct. 2023.
- [26] M. G. Ragab et al., "A comprehensive systematic review of YOLO for medical object detection," *IEEE Access*, vol. 12, pp. 57815–57836, 2024.
- [27] A. B. Amjoud and M. Amrouch, "Object detection using deep learning, CNNs and vision transformers: A review," *IEEE Access*, vol. 11, pp. 35479–35516, 2023.
- [28] G. Ghiasi, T.-Y. Lin, R. Pang, and Q. V. Le, "NAS-FPN: Learning scalable feature pyramid architecture for object detection," 2019, *arXiv:1904.07392*.
- [29] M. Lamane, M. Tabaa, and A. Klilou, "New approach based on Pix2Pix—YOLOv7 mmWave radar for target detection and classification," *Sensors*, vol. 23, no. 23, p. 9456, Nov. 2023.
- [30] Z. Chunlong, H. Peile, W. Shenghuai, W. Chen, and W. Hongxia, "Pavement defect detection algorithm based on improved YOLOv7 complex background," *IEEE Access*, vol. 12, pp. 32870–32880, 2024.
- [31] C. Li et al., "YOLOv6: A single-stage object detection framework for industrial applications," 2022, *arXiv:2209.02976*.

- [32] C.-Y. Wang, A. Bochkovskiy, and H.-Y. M. Liao, "Yolov7: Trainable bag-of-freebies sets new state-of-the-art for real-time object detectors," 2022, *arXiv:2207.02696*.
- [33] M. Ahmed, N. El-Sheimy, H. Leung, and A. Moussa, "Enhancing object detection in remote sensing: A hybrid YOLOv7 and transformer approach with automatic model selection," *Remote Sens.*, vol. 16, no. 1, p. 51, Dec. 2024.
- [34] P. Kumar et al., "Enhancing smart city safety and utilizing AI expert systems for violence detection," *Future Internet*, vol. 16, no. 2, p. 50, Jan. 2024.
- [35] W. Zhang et al., "Advances in tapered optical fiber sensor structures: From conventional to novel and emerging," *Biosensors*, vol. 13, no. 6, p. 644, Jun. 2023.
- [36] L. Macedo et al., "High-resolution sensors for mass deposition and low-frequency vibration based on phase-shifted Bragg gratings," *IEEE Sensors J.*, vol. 23, no. 3, pp. 2228–2235, Feb. 2023.
- [37] R. Singh, M. P. Ayyar, T. V. Sri Pavan, S. Gosain, and R. R. Shah, "Automating car insurance claims using deep learning techniques," in *Proc. IEEE 5th Int. Conf. Multimedia Big Data (BigMM)*, Sep. 2019, pp. 199–207.
- [38] P. Y. Anari et al., "Using YOLO v7 to detect kidney in magnetic resonance imaging," 2024, *arXiv:2402.05817*.
- [39] T. Balakrishnan and S. S. Sengar, "RepVGG-GELAN: Enhanced GELAN with VGG-STYLE convnets for brain tumour detection," 2024, *arXiv:2405.03541*.
- [40] A. Défossez, L. Bottou, F. Bach, and N. Usunier, "A simple convergence proof of Adam and Adagrad," 2022, *arXiv:2003.02395*.
- [41] X. Xie, P. Zhou, H. Li, Z. Lin, and S. Yan, "Adan: Adaptive Nesterov momentum algorithm for faster optimizing deep models," 2022, *arXiv:2208.06677*.
- [42] C. Zhang, Z. Hu, L. Xu, and Y. Zhao, "A YOLOv7 incorporating the adan optimizer based corn pests identification method," *Frontiers Plant Sci.*, vol. 14, Jun. 2023, Art. no. 1174556.
- [43] M. Hussain, H. Al-Aqrabi, M. Munawar, R. Hill, and T. Alsobou, "Domain feature mapping with YOLOv7 for automated edge-based pallet racking inspections," *Sensors*, vol. 22, no. 18, p. 6927, Sep. 2022.



**Pradeep Kumar** received the B.S. degree in information technology and the M.Tech. degree in computer science and engineering from Guru Gobind Singh Indraprastha University, Delhi, India, in 2019 and 2022, respectively. He is currently pursuing the Ph.D. degree in electro-optical engineering with the National Taipei University of Technology, Taipei, Taiwan.

His research interests include optical communication, fiber sensors, generative AI, deep learning, machine learning, and image processing.



**Cheng-Kai Yao** received the B.S. degree from the Department of Electro-Optical Engineering, National United University, Miaoli, Taiwan, in 2019. He is currently pursuing the Ph.D. degree with the Department of Electro-Optical Engineering, National Taipei University of Technology, Taipei, Taiwan.

His research interests include optic communication systems and fiber optic sensors



**Michael Augustine Arockiyadoss** received the B.Sc. degree in computer applications and the M.Sc. degree in computer science from St. Joseph's College, Tiruchirappalli, India, in 2020, and 2022, respectively. He is currently pursuing the Ph.D. degree with the Department of Electro-Optical Engineering, National Taipei University of Technology, Taipei, Taiwan.

His research focuses on optical fiber sensors, optical communication, IoT, and machine learning.



**Amare Mulatie Dehnaw** received the B.S. degree in information science from Jimma University, Jimma, Ethiopia, in 2012, the M.Sc. degree in information science from Addis Ababa University, Addis Ababa, Ethiopia, in 2015, and the Ph.D. degree in electrical engineering and computer science with the National Taipei University of Technology, Taipei, Taiwan, in 2023.

He is currently a Postdoctoral Researcher with the Department of Electro-Optical Engineering, National Taipei University of Technology. His research interests include fiber optic sensors, optical wireless communications, and deep learning.



**Ching-Yuan Chang** received the B.S. degree in mechanical engineering from National Chung-Hsing University, Taichung, Taiwan, in 2005, and the Ph.D. degree in mechanical engineering from the National Taiwan University, Taipei, Taiwan, in 2012.

He is currently an Associate Professor with the Mechanical Engineering Department, National Taipei University of Technology, Taipei. His research interests include solid mechanics, mechatronic systems, and precision measurement.



**Peng-Chun Peng** received the Ph.D. degree from the Institute of Electro-Optical Engineering, National Chiao Tung University, Hsinchu, Taiwan, in 2005.

He is currently a Full Professor and the Chairman with the Department of Electro-Optical Engineering, National Taipei University of Technology, Taipei, Taiwan. He has authored more than 150 journal articles and holds nine U.S. patents. His publications have been cited more than 4000 times, resulting in an H-index of 32.

Dr. Peng was invited as the Technical Program Committees for several prestigious conferences, including the Optical Fiber Communication Conference (OFC), OptoElectronics and Communications Conference (OECC), International Topical Meeting on Microwave Photonics (MWP), Asia Communications and Photonics Conference (ACP), and Wireless and Optical Communications Conference (WOCC).